Attosecond time-resolved streaked photoelectron spectroscopy of transition-metal nanospheres

Jianxiong Li, Erfan Saydanzad, and Uwe Thumm
Department of Physics, Kansas State University, Manhattan, Kansas 66506, USA
(Received 11 March 2017; published 25 April 2017)

Streaked photoemission from nanostructured surfaces and nanoparticles by attosecond extreme ultraviolet pulses into an infrared (IR) or visible streaking pulse allows for sub-fs-resolution of the plasmonically enhanced streaking-pulse electric field. It thus holds promise for the time-resolved imaging of the dielectric response in and plasmonic fields near nanostructures. After calculating the plasmonic field induced by IR and visible streaking pulses in 10- to 200-nm diameter Au, Ag, and Cu nanospheres, we numerically simulated streaked photoelectron spectra within a quantum-mechanical model. Our spectra show significant oscillation-amplitude enhancements and phase shifts relative to calculations that neglect the induced plasmonic field. We trace these observable effects to the distinct dielectric properties of the three investigated metals, demonstrating the applicability of streaking spectroscopy to the element-specific investigation of induced time-dependent electric fields near nanoparticle surfaces.

DOI: 10.1103/PhysRevA.95.043423

I. INTRODUCTION

Significant advances in nanoscience and technologies have enabled the design and synthesis of nanometer-sized structures with a tunable response to electromagnetic radiation [1–3]. Induced by the transient electric field of an incident laser pulse, this plasmonic response in metals is due to the electromagnetic field generated by the driven collective motion of conduction electrons. Near the surface of sub-wavelength-size isolated nanoparticles [4–6] and nanostructured surfaces [7–13], the induced plasmonic electromagnetic field can strongly enhance an incident inducing field, and the plasmonic near-field intensity can exceed the incident external-field intensity by several orders of magnitude [1]. Extreme plasmonic light-intensity amplification beyond 10^9 is being applied in well-established surface-enhanced Raman spectroscopy, allowing the spectroscopic characterization of individual molecules [14]. This huge light amplification forms the physical basis for promising new discipline-transcending techniques, such as attosecond nanoplasmonic-field microscopy [7], light harvesting [15], nanoplasmonically enhanced photocatalysis [16], and photothermal cancer therapy [17]. The continued unfolding of nanoplasmonic imaging techniques and nanoplasmonically enhanced devices is supported by recent theoretical [5,6,18–21] and experimental [4,22] efforts to help understand and detect induced plasmonic fields near nanostructures.

In parallel with the development of nanotechnologies over the past two decades, ultrafast laser technology has evolved to provide intense ultrashort pulses of electromagnetic radiation in the infrared (IR) and extreme ultraviolet (XUV) spectral range with pulse durations of a few femtoseconds (1 fs = 10^{-15} s) and a few tens of attoseconds (1 as = 10^{-18} s), respectively. In IR-IR and XUV-IR pump-probe experiments, pairs of such pulses can be synchronized, mutually delayed, and jointly focused on a target to allow the time-resolved investigation of the nuclear motion in small molecules [23–25] and electronic dynamics during the photoionization of atoms [26–29]. In contrast to sub-fs time-resolved photoemission studies on isolated atoms in the gas phase, experimental and theoretical time-domain investigations of the electronic dynamics in complex targets have been initiated more recently and are up to now limited to a small number of proof-of-principles studies [30,31]. The execution and theoretical analysis of time-resolved photoemission from nanotips [22,32], solid surfaces, and nanoparticles in sub-optical-cycle time-resolved streaking [6,31,33–36] and RABBITT (reconstruction of attosecond beating by interference of two-photon transitions) [37–41] experiments add challenges in preparing and characterizing clean and atomically flat solid surfaces and size- and shape-selected nanoparticles. Compared with photoemission from isolated gaseous atoms, numerical simulations of such experiments on complex targets require, in addition, the adequate modeling of (i) the complex electronic band structure [40,42], (ii) elastic and inelastic scattering of released photoelectrons inside the solid [34,42], the excitation of surface and bulk collective electronic excitations [43–45], (iii) the dielectric screening and reflection [41,46] of the assisting IR-laser field at the solid surface, (iv) the influence of equilibrating residual charge distributions on emitted photoelectrons [44],

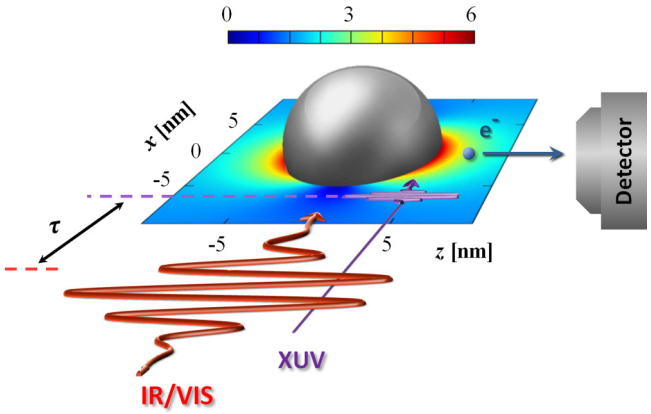

FIG. 1. Schematic of attosecond streaking from nanoparticles. A single ultrashort attosecond XUV pulse emits electrons into the field of a delayed IR or visible streaking laser pulse. The linear color or gray scale represents the maximal local electric-field-strength enhancement $\eta(\mathbf{r})$ [cf., Eq. (25)] in the x-z plane for the example of 10-nm diameter Ag nanospheres exposed to 720-nm incident IR pulses with peak intensity 10^{12} W/cm^2.

and (iv) the effect of spatially inhomogeneous plasmonic fields on the photoemission process [4–6,19–21,31].

The combination of modern nanoscience and ultrafast-laser technology holds promise for enabling improved and new methods for the imaging of the spatio-temporal dielectric response of nanostructures and new ultrafast electro-optical devices [7,18,30,31,47]. We here intend to contribute to this promising emerging field of research and development by employing a single-active-electron quantum-mechanical model [6,42] to the calculation of streaked XUV-photoemission spectra from Au, Ag, and Cu nanospheres (Fig. 1). We summarize our numerical model in Sec. II, which is subdivided into four subsections. These describe our calculation of the plasmonic $\mathbf{E}_{\rm plas}$ and total electric field $\mathbf{E}_{\rm tot}$ induced by the incident (visible or IR) streaking pulse within classical electrodynamics (Sec. II A), our quantum-mechanical modeling of the photoemission amplitude from a given initial valence-band state of the nanoparticle (Sec. II B), an approximated analytical evaluation of the time integration in our expression for the photoemission amplitude (Sec. II C), and our method for sampling over a large number of occupied initial states, required for the simulation of observable spectra (Sec. II D). In Sec. III we present our simulated streaked photoelectron spectra, starting with the discussion of the dependence of streaked spectra on the nanoparticle size and streaking-pulse wavelength in Sec. III A and following with the comparison of results from our quantum-mechanical calculation with two independent classical simulations [19,48] in Sec. III B. In Sec. III C we compare examples for the accurate quantitative retrieval of plasmonic-field information, followed by our conclusions in Sec. IV. Unless stated otherwise, we use atomic units (a.u.) throughout this work.

II. NUMERICAL MODEL

In our single-active-electron model, we study photoemission from the conduction band of a metallic (Au, Ag, or Cu) nanosphere of diameter D by isolated XUV pulses into the electric field of a delayed IR or visible streaking pulse (Fig. 1). We assume both pulses to be incident along the positive x axis and linearly polarized along the z axis of our coordinate system, the origin of which coincides with the center of the nanosphere. We designate the center-to-center IR-to-XUV pulse delay time as τ, such that XUV pulses precede the IR pulses for positive values of τ, and arbitrarily define the time $t = 0$ as the instant when the center of the XUV pulse passes the center of the nanosphere. In compliance with laser and XUV pulse parameters in typical streaking experiments, we further assume that (i) the XUV pulse length τ_X is significantly shorter than an optical cycle of the streaking pulse, and (ii) the intensity of the streaking pulse is too small to induce photoemission from the target or to noticeably perturb the nanosphere's electronic structure, thus merely causing a delay-dependent shift of the photoelectron's final kinetic energy $\varepsilon_f(\tau)$ [31]. This energy shift is observable by streaked photoemission spectroscopy and carries information on the total electric field $\mathbf{E}_{\rm tot}$ near the nanosphere surface. $\mathbf{E}_{\rm tot}$ is given by the incident streaking field $\mathbf{E}_{\rm inc}$ and the spatially inhomogeneous induced plasmonic field $\mathbf{E}_{\rm plas}$.

A. Induced plasmonic response to the streaking field

For any given spectral component of the incident streaking pulse,

$$\mathbf{E}_{\rm inc}(\mathbf{r},t;\omega) = \hat{\mathbf{z}}E_0(\omega)e^{i(kx-\omega t)}, \tag{1}$$

the corresponding spectral component of the total electric field,

$$\begin{aligned}\mathbf{E}_{\rm tot}(\mathbf{r},t;\omega) &= \mathbf{E}_{\rm inc}(\mathbf{r},t;\omega) + \mathbf{E}_{\rm plas}(\mathbf{r},t;\omega)\\ &= \mathbf{E}_{\rm tot,0}(\mathbf{r};\omega)e^{i\phi_{\rm tot}(\mathbf{r};\omega)}e^{i(kx-\omega t)},\end{aligned} \tag{2}$$

is obtained by solving Maxwell's equations. This is done by expressing both the incident and plasmonic field in terms of an infinite series expansion and by determining the expansion coefficients by applying the appropriate boundary conditions at large distances from the nanosphere and for the normal and tangential total electric-field components at the nanosphere surface following the work of Mie [49,50]. The phase factor $\phi_{\rm tot}(\mathbf{r};\omega)$ is defined so that the z component of $\mathbf{E}_{\rm tot,0}(\mathbf{r},t;\omega)$ is real. $\phi_{\rm tot}(\mathbf{r};\omega)$ thus constitutes the spectral phase shift of the plasmonically enhanced incident streaking pulse relative to the incident plane-wave component $\mathbf{E}_{\rm inc}(\mathbf{r},t;\omega)$ with real amplitude $E_0(\omega)$.

The dielectric properties of the nanosphere materials are given by the complex permittivity $\epsilon(\omega) = \tilde{n}(\omega)^2$ or, alternatively, the complex index of refraction $\tilde{n}(\omega)$, for which we adopt the experimental values for bulk Au, Ag, and Cu of Ref. [51]. Figures 2(a)–2(c) show the real and imaginary components of the permittivity for Au, Ag, and Cu, respectively. Two distinguishable frequency domains can be identified in these figures [52,53]: the "free-electron region" (white) at

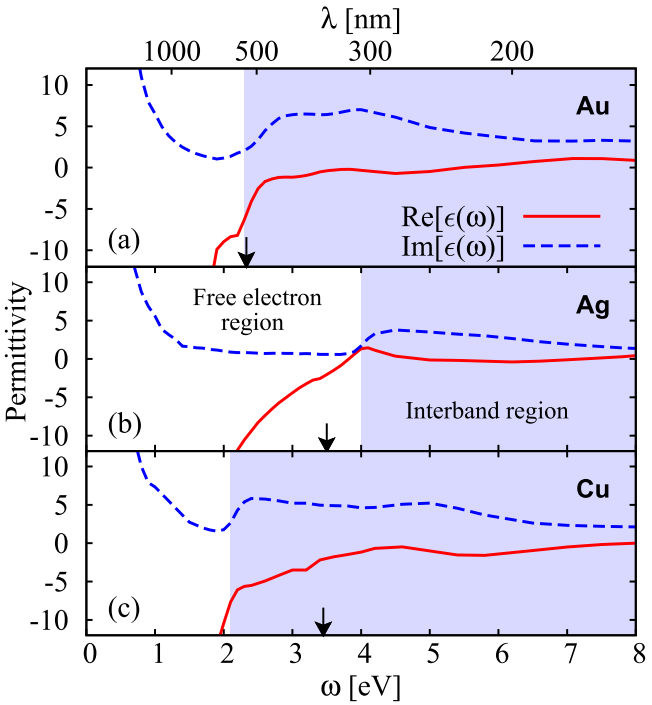

FIG. 2. Real and imaginary components of the complex permittivity $\epsilon(\omega)$ for Au, Ag, and Cu (adapted from Ref. [51]). The white and shaded areas indicate free-electron and interband-transition regions, respectively. Arrows point to the dipole surface-plasmon frequencies ω_D of subwavelength nanoparticles for each material.

low frequencies and the "interband region" (shaded) at higher frequencies. In the free-electron region the incident field oscillates sufficiently slowly for conduction electrons to behave like free electrons as described by the Drude model [54]. In this domain, $|\mathrm{Re}[\epsilon(\omega)]|$ and $|\mathrm{Im}[\epsilon(\omega)]|$ decrease as the frequency of the incident field increases, followed by a strong increase of $\mathrm{Im}[\epsilon(\omega)]$ near the threshold of interband transitions at frequency ω_I. The interband-transition-threshold frequencies (wavelengths) are approximately 2.3 eV (530 nm) for Au, 4.0 eV (310 nm) for Ag, and 2.1 eV (580 nm) for Cu. In the interband region, the loss function $-\mathrm{Im}[\epsilon(\omega)]^{-1}$ tends to be large, indicating the likely loss of photon energy to interband excitations [52].

For subwavelength nanoparticles ($D << \lambda$) the quasistatic electric-field approximation applies. Within this approximation, the dipole surface plasmon frequency ω_D, i.e., the natural frequency of the induced collective electron oscillation, can be obtained at the maximal polarizability of the nanoparticle according to the Fröhlich condition [54]:

$$\mathrm{Re}[\epsilon(\omega_D)] = -2\epsilon_m, \tag{3}$$

where ϵ_m (=1) is the permittivity of the surrounding medium (vacuum in this study). The dipole surface plasmon frequencies $\omega_D = 2.3\,\mathrm{eV}$ (530 nm) for Au, 3.4 eV (360 nm) for Ag, and 3.3 eV (375 nm) for Cu are indicated as arrows in Figs. 2(a), 2(b), and 2(c), respectively. The resonant behavior of the polarizability at ω_D also depends on $\mathrm{Im}[\epsilon(\omega)]$ and tends to be most pronounced for small or slowly varying $\mathrm{Im}[\epsilon(\omega)]$ in the free-electron region. In contrast, the resonant polarization enhancement may be suppressed and hardly, if at all, recognizable if ω_D lies in the interband region: While the polarization enhancement in Ag is characterized by a pronounced resonance in the free-electron region at ω_D, for Cu ω_D—as determined based on the real part of $\epsilon(\omega)$ only according to (3)—lies in the interband region where interband excitations damp the surface-plasmon resonance and strongly red-shift ω_D to a broad resonance near ω_I. These profound differences in the dielectric response of Au, Ag, and Cu

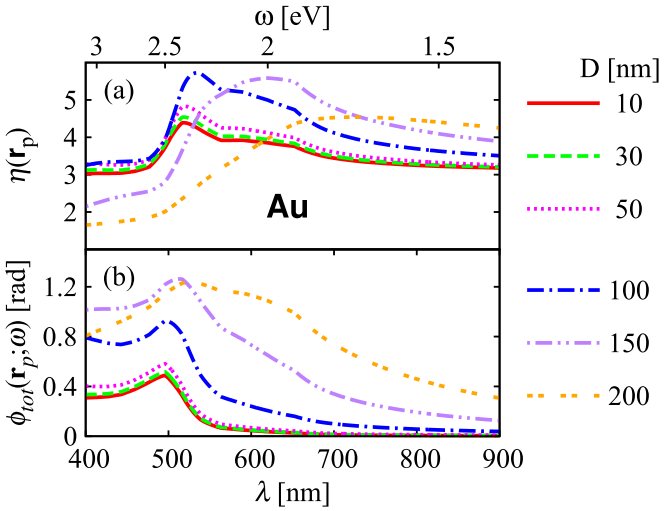

FIG. 3. (a) Plasmonic field enhancement $\eta(\mathbf{r}_p)$ and (b) phase shift $\phi_{\mathrm{tot}}(\mathbf{r}_p;\omega)$ at the electric-field poles $\mathbf{r}_p$ on Au nanospheres with diameters D as a function of the incident plane wave's wavelength λ.

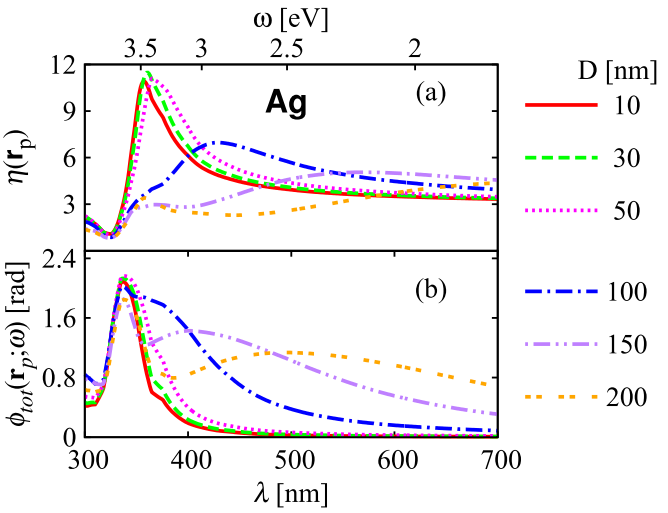

FIG. 4. Same as Fig. 3 for Ag nanospheres.

are reflected in the calculated electric-field enhancements discussed next.

The ratio of the total and incident electric-field intensity,

$$\eta(\mathbf{r}) = |\mathbf{E}_{\mathrm{tot},0}(\mathbf{r};\omega)|/E_0, \tag{4}$$

defines the plasmonic electric-field enhancement. By calculating the total electric field within Mie theory [49,50], we find the largest electric-field enhancement $\eta(\mathbf{r}_p)$ at the electric-field "poles" [$\mathbf{r}_p = (0,0,z_p)$] of the nanosphere along the IR and XUV polarization direction shown in Fig. 1. Figures 3(a), 4(a), and 5(a) show $\eta(\mathbf{r}_p)$ as a function of the incident pulse wavelength $\lambda = 2\pi/k = 2\pi c/\omega$ for 10- to 200-nm diameter Au, Ag, and Cu nanospheres, respectively, where c is the speed of light in vacuum.

For nanosphere diameters smaller or equal to $D = 100\,\mathrm{nm}$, Au displays a pronounced plasmon resonance at $\lambda = 530\,\mathrm{nm}$ ($\omega = 2.3$ eV) [Fig. 3(a)]. In light of the preceding discussion, this can be expected, since ω_D is just at the threshold for interband excitations ω_I. The largest enhancement factor of $\eta(\mathbf{r}_p) \approx 6$ is found for $D = 100\,\mathrm{nm}$. For Ag, on the other hand,

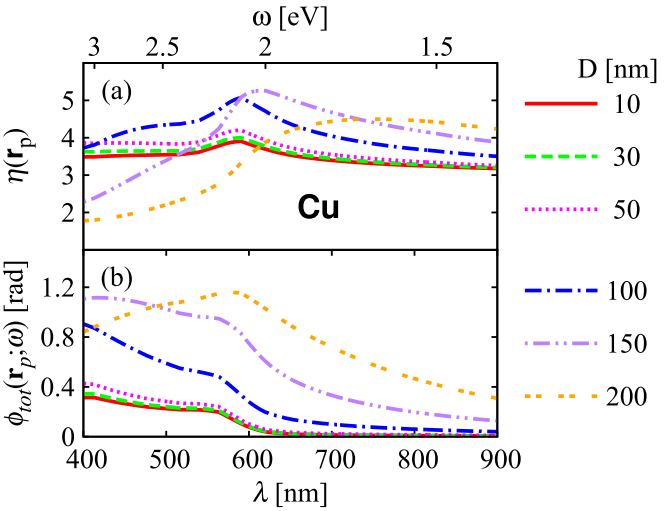

FIG. 5. Same as Fig. 3 for Cu nanospheres.

$\omega_D = 3.4$ eV lies within the free-electron region and is well separated from ω_I [Fig. 4(a)]. Accordingly, Ag nanoparticles have a comparatively narrow (undamped) plasmon resonance near 360 nm (3.4 eV) with large amplitude enhancement. We find the largest enhancement $\eta(\mathbf{r}_p) \approx 6$ for $D = 30$ nm. Silver has the largest enhancement among the three transition metals compared in this work. For Cu, in sharp contrast to Ag, $\omega_D = 3.3$ eV lies deeply within the interband region. Consequently, the enhancement maximum for Cu nanospheres is strongly red-shifted from ω_D to the interband-transition threshold and appears as a very broad resonance profile in Fig. 5(a). The strongest enhancement $\eta(\mathbf{r}_p) \approx 5$ occurs near 580 nm (2.1 eV) for $D = 100$ nm.

For Au, Ag, and Cu nanopheres with diameters larger than $D = 100$ nm, the maximal-enhancement frequencies are strongly red-shifted and the enhancement maxima are smaller as compared to particles with $D < 100$ nm [Figs. 3(a), 4(a), and 5(a)]. This is due to the fact that as D approaches λ, the quasistatic approximation begins to fail, such that Eq. (3) is no longer valid. These large size-dependent red-shifts are accounted for by corrections to the Fröhlich condition (3) [54] and are confirmed by strongly red-shifted size-dependent absorption peaks in measured photoabsorption spectra [55]. These size-dependent red-shifts are also in full compliance with the intuitively expected red-shift of confinement resonances in quantum wells of increasing width [cf. Fig. 2 in Ref. [56]].

The local phase shift $\phi_{\rm tot}(\mathbf{r}_p;\omega)$ at the poles $\mathbf{r}_p$ of the total electric field $\mathbf{E}_{\rm tot}(\mathbf{r}_p,t;\omega)$ (2) relative to the incident field $\mathbf{E}_{\rm inc}(\mathbf{r}_p,t;\omega)$ (1) is shown in Figs. 3(b), 4(b), and 5(b) for Au, Ag, and Cu nanospheres, respectively. For Au and Ag, the size and material dependence of the plasmon resonance appears in $\phi_{\rm tot}(\mathbf{r}_p;\omega)$ in the same fashion as in the field enhancement $\eta(\mathbf{r}_p)$, while for Cu the broad plasmon resonance visible in $\eta(\mathbf{r}_p)$ near $\lambda = 580$ nm in Fig. 5(a) translates into a more rapid decrease of $\phi_{\rm tot}(\mathbf{r}_p;\omega)$ in Fig. 5(b). The maximal phase shifts in Figs. 3(b), 4(b), and 5(b) are $\phi_{\rm tot}(\mathbf{r}_p;\omega) \approx 1.3$ rad for Au, 2.1 rad for Ag, and 1.2 rad for Cu. These phase shifts correspond to time delays of the wavefronts of the plasmonically enhanced spectral components (2) relative to the plane waves (1) of 360 as for Au, 400 as for Ag, and 370 as for Cu. For $\lambda \gg D$ the phase shift vanishes, as expected, since conduction electrons respond adiabatically to sufficiently slow external field oscillations.

The plasmonically enhanced streaking pulse is given by the superposition of its spectral components (2),

$$\mathbf{E}_{\rm tot}(\mathbf{r},t) = \int d\omega\ \mathbf{E}_{{\rm tot},0}(\mathbf{r};\omega) e^{i\phi_{\rm tot}(\mathbf{r};\omega)} e^{-i\omega t}. \tag{5}$$

In our numerical applications below, we consider incident streaking pulses,

$$\mathbf{E}_{\rm inc}(\mathbf{r},t) = \int d\omega\ \mathbf{E}_{\rm inc}(\mathbf{r};\omega), \tag{6}$$

with Gaussian temporal profiles, 2.47-fs full width at half maximum (FWHM) intensity, corresponding to a spectral width of $\Gamma_{\rm inc} = 0.73$ eV, and a peak intensity of 10^{12} W/cm^2.

TABLE I. Work functions, conduction-band widths, and mean-free paths (MFP) for Au, Ag, and Cu.

	Work function (eV)	Bandwidth (eV)	MFP (Å)
Au	5.1 [58]	8 [59]	4.4 [60]
Ag	4.5 [58]	8 [59]	4.9 [60]
Cu	4.7 [58]	6 [61]	5.1 [60]

B. Quantum-mechanical photoemission amplitude

In typical streaking experiments, electrons are emitted upon absorption of a single photon of the ionizing isolated XUV pulse [31]. We assume XUV pulses with a Gaussian temporal profile,

$$\mathbf{E}_X(\mathbf{r},t) = \hat{\mathbf{z}} E_X \exp\left[-2\ln 2\left(\frac{t-t_x}{\tau_X}\right)^2\right] e^{-i\omega_X(t-t_x)}, \tag{7}$$

a central photon energy of $\omega_X = 105$ eV, and (unless specified otherwise) a pulse length (FWHM intensity) of $\tau_X = 200$ as, where $t_x = x/c$. We further may assume that the nanosphere is transparent to the XUV pulses, since $\tilde{n}(\omega_X) \approx 1$ at XUV frequencies [51]. Thus, the vector potential of the XUV pulse can be written in Coulomb gauge as

$$\mathbf{A}_X(\mathbf{r},t) = \int_t^\infty dt'\ \mathbf{E}_X(\mathbf{r},t'). \tag{8}$$

The quantum-mechanical transition amplitude for single-XUV-photon emission of an electron from an initial state Ψ_i into the final state $\Psi^\tau_{\mathbf{k}_f}$ in the velocity gauge as a function of the final photoelectron momentum $\mathbf{k}_f$ and time delay τ is given by [6,57]

$$T_i(\mathbf{k}_f,\tau) = i \int dt \int d\mathbf{r} \Psi^{\tau *}_{\mathbf{k}_f}(\mathbf{r},t) \mathbf{A}_X(\mathbf{r},t)\cdot\hat{\mathbf{p}}\Psi_i(\mathbf{r},t), \tag{9}$$

where $\hat{\mathbf{p}} = -i\nabla$ is the electron momentum operator. We model initial conduction-band states,

$$\Psi_i(\mathbf{r},t) = \Psi_i(\mathbf{r}) e^{-i\omega_i t}, \tag{10}$$

as bound states of a spherical square well of radius $D/2$ and set the depth of the spherical square-well potential equal to the sum of the work function and conduction-band width. The work function and conduction-band width used in our numerical simulations for Au, Ag, and Cu are listed in Table I. We represent the final continuum state as the exponentially damped "Volkov" continuum wave function [6],

$$\Psi^\tau_{\mathbf{k}_f}(\mathbf{r},t) = \frac{1}{\sqrt{2\pi}} f[l(\mathbf{r});\lambda_i)] e^{i\mathbf{k}_f\cdot\mathbf{r}} e^{i\phi^\tau_{\mathbf{k}_f}(\mathbf{r},t)}, \tag{11}$$

with the position-dependent generalized Volkov phase,

$$\phi^\tau_{\mathbf{k}_f}(\mathbf{r},t) = \int_t^\infty dt' \mathbf{p}^2(\mathbf{r},t')/2. \tag{12}$$

The damping factor $f(l;\kappa) = \exp[-l/(2\kappa)]$ accounts for scattering of the photoelectron inside the nanoparticle after being excited ("born") by the XUV pulse at position $\mathbf{r}$. Due to scattering, photoelectrons born inside the nanosphere are less likely to be registered by the detector (Fig. 1). In addition to the inelastic mean free path (MFP) κ, the damping factor

depends on the path length $l(\mathbf{r})$ of photoelectrons inside the nanosphere. κ changes by about 2% for the energy range and pulse parameters and for each of the three transition metals considered in this work. We can therefore neglect its dependence on the photoelectron kinetic energy and consider it as constant. The MFPs used for our numerical simulations are listed in Table I. We calculate the path length $l(\mathbf{r})$ numerically, based on classical photoelectron trajectories $\tilde{\mathbf{r}}(t')$ with initial positions $\tilde{\mathbf{r}}(t) = \mathbf{r}$ at time t and initial momenta,

$$\mathbf{p}(\mathbf{r},t) = \mathbf{k}_f + \int_t^\infty dt'\ \mathrm{Re}\mathbf{E}_{\mathrm{tot}}[\tilde{\mathbf{r}}(t'),t']. \tag{13}$$

C. Evaluation of the photoemission amplitude

The central energy of the XUV pulses (7) assumed in this work (105 eV) corresponds to an optical period of 39.39 as. This period being significantly shorter than the XUV-pulse duration ($\tau_X = 200$ as) allows the representation of the XUV-pulse vector potential (8) in slowly-varying-amplitude approximation as the Gaussian pulse,

$$\begin{aligned}\mathbf{A}_X(\mathbf{r},t) &= \int_t^\infty dt'\ \mathbf{E}_X(\mathbf{r},t') \\ &\approx -\hat{\mathbf{z}}\frac{iE_X}{\omega_X}\exp\left[-2\ln 2\left(\frac{t-t_x}{\tau_X}\right)^2\right]e^{-i\omega_X(t-t_x)}.\end{aligned} \tag{14}$$

Thus, even though the time integral in Eq. (9) extends over the entire real axis, noticeable contributions to it only arise near the center of the XUV pulse at $t = t_X$.

The visible and IR streaking pulses we consider have wavelengths between 350 and 800 nm. Their corresponding optical cycles lie between 1.06 and 2.66 fs and are significantly longer than the XUV pulse duration. Compared to the envelope of the XUV pulse, the temporal variation of the streaking field and generalized Volkov phase (12) is thus very slow. Consistent with the remark following Eq. (14), we therefore Taylor expand (12) as a function of time about t_x,

$$\begin{aligned}\phi^\tau_{\mathbf{k}_f}(\mathbf{r},t) &= \phi^\tau_{\mathbf{k}_f}(\mathbf{r},t_x) + \phi^{\tau\,\prime}_{\mathbf{k}_f}(\mathbf{r},t_x)(t-t_x) \\ &\quad + \frac{1}{2}\phi^{\tau\,\prime\prime}_{\mathbf{k}_f}(\mathbf{r},t_x)(t-t_x)^2 + O((t-t_x)^3),\end{aligned} \tag{15}$$

where the primes refer to time derivatives. Equation (9) then becomes

$$\begin{aligned}T_i(\mathbf{k}_f,\tau) &= -\frac{iE_X}{\omega_X}\hat{\mathbf{z}}\cdot\int d^3\mathbf{r}\,[\nabla\Psi_i(\mathbf{r})]\Psi^{\tau *}_{\mathbf{k}_f}(\mathbf{r},t_x)e^{-i\omega_i t_x} \\ &\quad\times\int dt\exp\left[-\left(\frac{2\ln 2}{\tau_X^2}+\frac{i}{2}\phi^{\tau\,\prime\prime}_{\mathbf{k}_f}(\mathbf{r},t_x)\right)(t-t_x)^2\right] \\ &\quad\times e^{-i(\phi^{\tau\,\prime}_{\mathbf{k}_f}(\mathbf{r},t_x)+\omega_X+\omega_i)(t-t_x))}.\end{aligned} \tag{16}$$

The time integral now represents the Fourier transformation of a Gaussian function and can be performed analytically with the result,

$$\begin{aligned}T_i(\mathbf{k}_f,\tau) &= \frac{\sqrt{\pi}E_X}{i\omega_X}\hat{\mathbf{z}}\cdot\int d^3\mathbf{r}\,[\nabla\Psi_i(\mathbf{r})]\Psi^{\tau *}_{\mathbf{k}_f}(\mathbf{r},t_x)e^{-i\omega_i t_x} \\ &\quad\times\frac{1}{b^\tau_{\mathbf{k}_f}(\mathbf{r})}\exp\left[-\left(\frac{\phi^{\tau\,\prime}_{\mathbf{k}_f}(\mathbf{r},t_x)+\omega_X+\omega_i}{2b^\tau_{\mathbf{k}_f}(\mathbf{r})}\right)^2\right],\end{aligned} \tag{17}$$

where

$$b^\tau_{\mathbf{k}_f}(\mathbf{r}) = \sqrt{\frac{2\ln 2}{\tau_X^2}+\frac{i}{2}\phi^{\tau\,\prime\prime}_{\mathbf{k}_f}(\mathbf{r},t_x)}. \tag{18}$$

We perform the three remaining integrations in Eq. (17) numerically. In numerical tests we confirmed that the approximation (16) to the amplitude (9) does not induce noticeable changes in any of the numerical results shown and discussed in Sec. III below.

D. Summation over initial states

Eq. (17) gives the transition amplitude for photoemission out of a particular initial state Ψ_i. Allowing for photoelectron emission from any occupied conduction-band state, we incoherently add contributions to the total photoelectron yield from initial states with energies ε_i at and below the Fermi energy,

$$P(E_f,\tau) = \sum_{i\in\mathrm{occ}}|T_i(\mathbf{k}_f,\tau)|^2. \tag{19}$$

Electronic confinement in nanometer-size objects results in a very large number of energetically very narrowly spaced initial conduction-band states. For example, a $D = 10$ nm Au nanosphere, the smallest diameter considered in our numerical applications below, contains 26 551 bound states with maximal angular-momentum quantum number $l_{\max} = 65$ below the Fermi level, and this number increases with the size of the nanosphere. We therefore carried out the summation in Eq. (19) by dividing the conduction band into m equal segments, $S_j = 1,....m$, each segment having $n(j)$ occupied states. Eq. (19) can then be rewritten as

$$\begin{aligned}P(E_f,\tau) &= \sum_{j=1}^m n(j)\times\left[\frac{1}{n(j)}\sum_{i\in S_j}|T_i(\mathbf{k}_f,\tau)|^2\right] \\ &= \sum_{j=1}^m n(j)\times P_j(E_f,\tau),\end{aligned} \tag{20}$$

where $P_j(E_f,\tau)$ is the average yield in segment S_j.

For numerical efficiency, we evaluated Eq. (20) approximately by replacing $P_j(E_f,\tau)$ with the averaged yield in segment S_j,

$$P^{\mathrm{ave}}_j(E_f,\tau) = \frac{1}{q}\sum_{i=1}^q|T_{[N(i)*n(j)]}(\mathbf{k}_f,\tau)|^2. \tag{21}$$

We obtained $P^{\mathrm{ave}}_j(E_f,\tau)$ by calculating the transition amplitude for q randomly sampled occupied states in S_j, with the sampling function $N(i)$ returning uniformly distributed random numbers in the interval $[0,1]$. For $m = 10$ and $q = 10$ and all numerical examples discussed in this work, we found Eq. (21) to approximate the photoemission yields (19) with a relative error below 5%.

III. STREAKED PHOTOELECTRON SPECTRA

In this section, we discuss our simulated streaked photoelectron spectra for Au, Ag, and Cu nanospheres with diameters of 10 and 50 nm. For each material, we consider two streaking-pulse wavelengths of 720 nm and the respective

plasmonic-enhancement-resonance wavelength (530 nm for Au, 360 nm for Ag, and 580 nm for Cu).

A. Size and streaking-wavelength dependence

Figures 6–8 show our numerical results for streaked photoemission spectra from Au, Ag, and Cu nanospheres, respectively. The streaking traces oscillate with amplitudes $\delta\varepsilon_f(D,\lambda)$ due to the XUV-IR-pulse-delay-dependent energy shift imposed by the total electric field $\mathbf{E}_{\rm tot}$ (5) on the emitted electron. Their delay dependence thus resembles the temporal profile of $\mathbf{E}_{\rm tot}$ as explained above, relative to which they are phase shifted [6,19,31]. $\delta\varepsilon_f(D,\lambda)$ varies with the size of the nanosphere and the center wavelength of the streaking pulse. Independent of the transition metal investigated, $\delta\varepsilon_f(D,\lambda)$ increases with the size of the nanosphere for a given streaking-pulse wavelength, consistent with and proportional to the respective size-dependent plasmonic enhancements shown in Figs. 3(a), 4(a), and 5(a).

With regard to the streaking-pulse-wavelength dependence, $\delta\varepsilon_f(D,\lambda)$ remains approximately the same for 720 and 530 nm Au nanospheres of a given diameter, as the comparison of Fig. 6(a) with Fig. 6(b) and of Fig. 6(c) with Fig. 6(d) demonstrates. This wavelength-independence of the streaking amplitude disagrees with a well-known common feature of streaked photoelectron spectra from gaseous atomic targets [31], for which the streaking-oscillation amplitude,

$$\delta\varepsilon_f(D,\lambda) \sim \lambda E_0, \tag{22}$$

is proportional to the incident wavelength and incident streaking field amplitude, resulting in larger oscillation amplitudes for larger wavelength. The approximate λ independence of

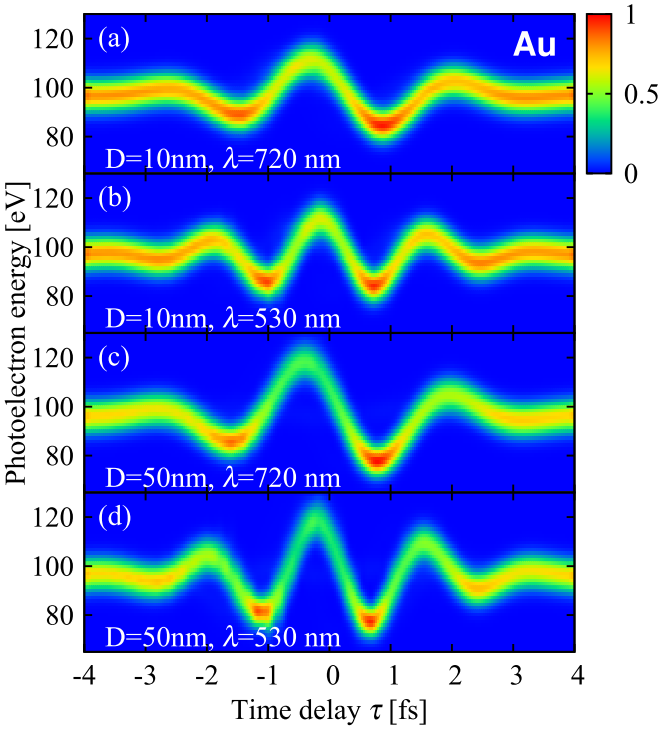

FIG. 6. Quantum-mechanically calculated streaked XUV photoemission spectra for 10- and 50-nm diameter Au nanospheres and streaking-field wavelengths of 720 and 530 nm. The linear color or gray scale gives the photoemission yield separately normalized to the maximal yields in (a)–(d).

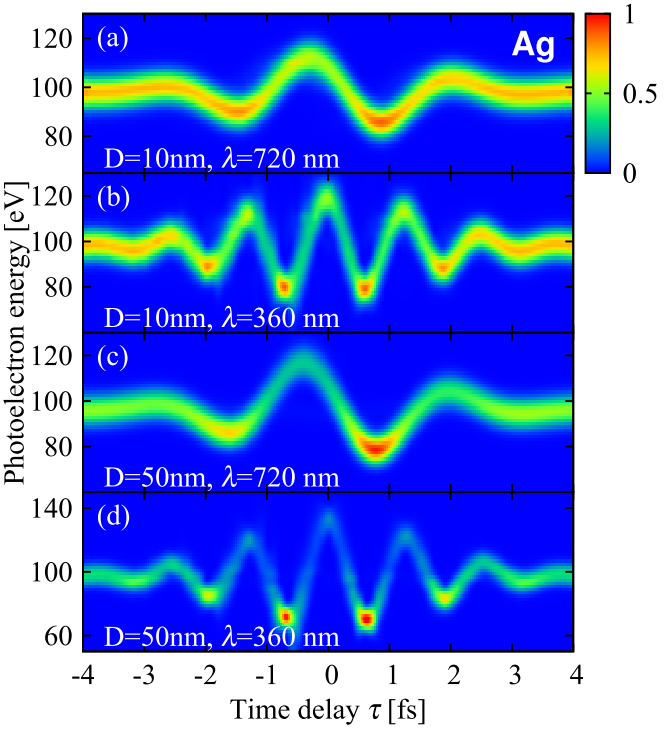

FIG. 7. Same as Fig. 6 for Ag nanospheres and streaking-field wavelengths of 720 and 360 nm.

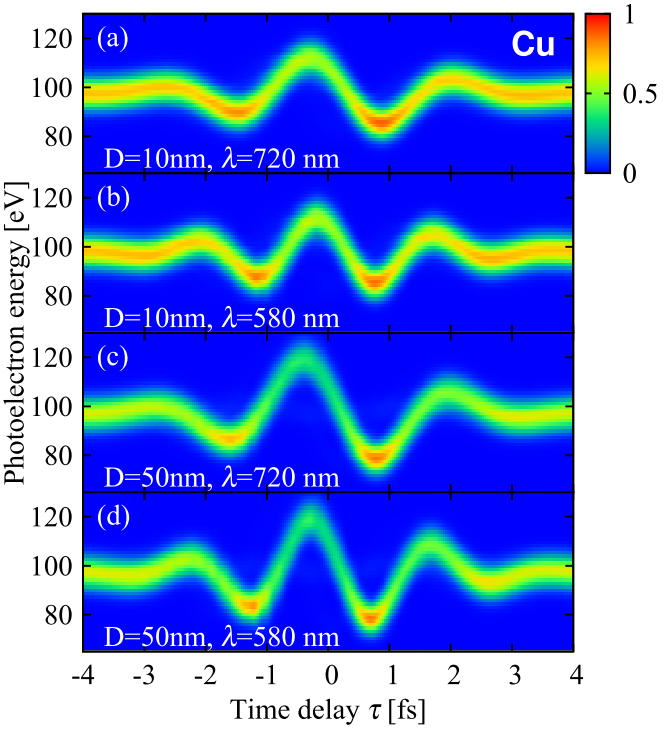

FIG. 8. Same as Fig. 6 for Cu nanospheres and streaking-field wavelengths of 720 and 580 nm.

$\delta\varepsilon_f(D,\lambda)$ for Au nanospheres is due to the cancelation of two effects: While the λ dependence in Eq. (22) carries over from gaseous atoms to nanospheres, the incident-streaking-pulse amplitude E_0 needs to be replaced by the amplitude of the plasmonically enhanced streaking field (5) at the nanoparticle surface,

$$\delta\varepsilon_f(D,\lambda) \sim \lambda|\mathbf{E}_{\mathrm{tot},0}|. \tag{23}$$

According to Fig. 6, the plasmonic-field enhancement at 720 nm is weaker than for 530 nm (Fig. 3) and (accidentally) happens to balance the increase of $\delta\varepsilon_f(D,\lambda)$ with λ found for gaseous atomic targets. The degree of sensitivity of the streaking-trace amplitude to the nanoparticle size is thus indicative for plasmonic-field enhancement at the nanoparticle surface.

We find the same approximate independence of the streaking amplitude on the streaking wavelength for 10 and 50 nm Cu nanospheres (Fig. 8). For a given diameter, Cu nanospheres reveal approximately the same streaking-oscillation amplitude $\delta\varepsilon_f(D,\lambda)$ as Au nanospheres, both on resonance (580 nm) and off-resonance (720 nm). In contrast, the apparent streaking amplitude for 10 and 50 nm Ag nanospheres is noticeably larger near the plasmon-resonance wavelength (360 nm) than off-resonance at 720 nm (Fig. 7). The less-then-perfect cancellation of the λ dependence of the two factors in Eq. (23) for Ag nanospheres is an expression of the (i) polarizability of Ag being much larger than the polarizability of Au and Cu and (ii) strong material dependence of the streaking amplitude.

Figures 6–8 show pronounced maxima of the photoemission yield at the lowest photoelectron energies, i.e., at the energetic minima of the streaking traces. This energy-dependent variation in photoemission yield is consistent with the known monotonic decrease of the XUV-photoemission cross section $\sigma(\epsilon_f)$ with the photoelectron energy in the absence of resonances [57] [cf. Fig. 9(e) below]. The contrast between photoemission yields at maximal positive and negative streaking energy shifts $\delta\varepsilon_f(D,\lambda)$ thus tends to increase with the streaking amplitude. Since the streaking amplitude depends on the streaking wavelength, the nanoparticle size, and its material, as discussed above, the maximal emission-yield contrast as a function of the time delay τ is different for the four wavelengths, three transition metals, and two particle sizes examined in Figs. 6–8.

B. Comparison with classical calculations

In Fig. 9 we compare streaked photoelectron spectra for 10-nm diameter Au nanospheres and 720-nm streaking-field wavelength, resulting from independently performed classical-trajectory Monte Carlo simulations of Süßmann and Kling [19] and Saydanzad *et al.* [48], with our quantum-mechanical simulation. For this comparison only, we changed the XUV-pulse length from 200 to 287 as, in order to employ the same XUV parameters as in the two classical calculations. The classical spectra in Figs. 9(b) and 9(c) are calculated for the same streaking and XUV parameters used in our numerical model [Fig. 9(a)]. At a first glance, the classical and quantum-mechanical results in Figs. 9(a)–9(c) appear to be in good agreement, however, examination of their centers of energy (CoE) reveals three noticeable differences:

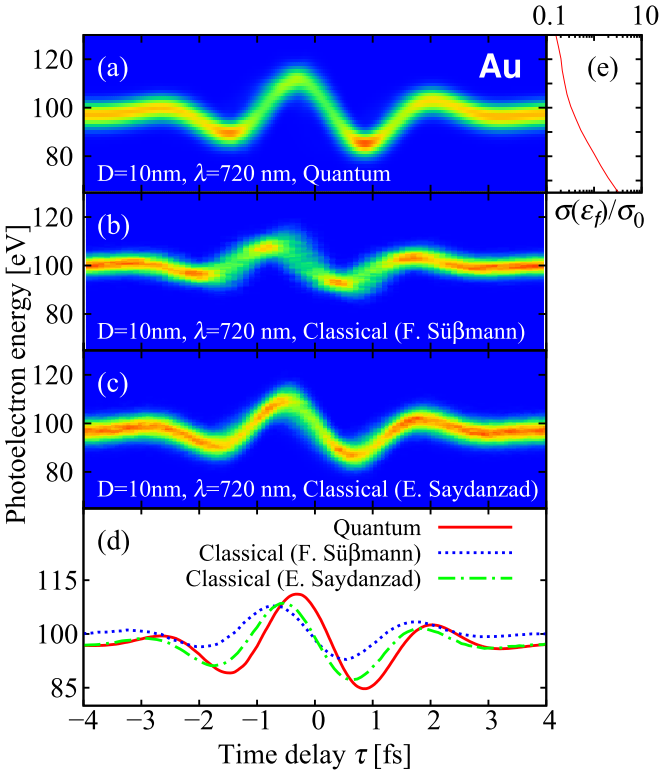

FIG. 9. Calculated streaked XUV photoemission spectra for 10-nm diameter Au nanospheres and streaking-field wavelengths of 720 nm according to (a) our quantum-mechanical model, (b) the classical model of Süßmann and Kling (adapted from Ref. [19]), and (c) the classical model of Saydanzad *et al.* (adapted from Ref. [48]). The linear color or gray scale gives the photoemission yield normalized to the maximal yield for each plot. (d) Centers of energy of the spectra in (a)–(c). (e) XUV-photoionization cross section $\sigma(\varepsilon_f)$, normalized at $\sigma_0 = \sigma(80\,\mathrm{eV})$.

First, the CoE in the classical simulation by Süßmann and Kling lies approximately 4 eV higher than in the two other calculations. This is a result of the classical model in Ref. [19] being restricted to photoemission from the Fermi level only, while both our quantum-mechanical model and the classical model in Ref. [48] allow for photoemission from all occupied conduction-band states.

Second, the energy dependence of the photoemission yield as a function of the XUV-IR-pulse delay is different for all three simulations. Consistent with the photoelectron-energy dependence of the quantum-mechanically calculated XUV-photoemission cross section $\sigma(\varepsilon_f)$ [57] shown in Fig. 9(e), the energy dependence of the quantum-mechanical streaking spectrum in Fig. 9(a) strongly emphasizes photoemission at lower energies. This effect is absent in both classically calculated spectra.

Third, streaking amplitudes and streaking phases predicted by all three calculations are noticeably different, as shown for the CoE of all spectra in Fig. 9(d). The quantum-mechanical model predicts the largest and the classical model in Ref. [19] the smallest oscillation amplitude. The difference between the two classical calculations appears to be due to different model assumptions. While the classical calculations of Saydanzad *et al.* [48] allow for photoelectron release from

inside the nanoparticle with a dipolar angular distribution and include electron scattering of released photoelectrons inside the nanosphere, the classical model of Ref. [19] restricts conduction-band-electron release to the surface, does not allow for scattering of photoreleased electrons inside the nanoparticle, and assumes photoemission probabilities that do not depend on the emission location on the sphere. To some extent the differences in the classical and quantum-mechanical CoE streaking amplitudes and phases are due to fundamental dissimilarities of classical and quantum-mechanical dynamics, such as the inclusion or absence of coherence in quantum or classical calculations.

C. Plasmonic-field-information retrieval

In order to investigate the extent to which plasmonic field information is imaged in streaked photoelectron spectra, we calculated streaked spectra with and without including the induced plasmonic field $\mathbf{E}_{\rm plas}(\mathbf{r},t)$ in Eq. (2), while leaving all nanosphere, XUV-, and IR-pulse parameters unchanged. The CoE of these spectra for 10 nm Au, Ag, and Cu nanospheres and various wavelengths are shown in Fig. 10. They reveal a significant increase and phase shift of the streaking amplitude due to the induced plasmonic field.

In order to retrieve the plasmonic-field enhancement and phase shift, we fit our numerically calculated CoE to a sinusoidal function with Gaussian envelope,

$$\varepsilon(\tau) = \varepsilon_0 + A\exp\left[-2\ln 2\left(\frac{\tau}{\sigma}\right)^2\right]\cos(\omega\tau+\phi), \qquad (24)$$

and adjust the values of $\varepsilon_0, A, \sigma, \omega, \phi$. To quantify the effects of the plasmonic-field enhancement on streaked spectra, we introduce the *wave-length-resolved* (spectral) streaking-oscillation-amplitude-enhancement factor,

$$\eta_{\rm streak}(\lambda) = \left.\frac{A_w}{A_{w/o}}\right|_{\lambda}, \qquad (25)$$

where A_w and $A_{w/o}$ are the oscillation amplitudes adjusted according to Eq. (24) with and without including the induced plasmonic field, respectively. We further define the spectral phase-shift difference,

$$\Delta\phi_{\rm streak}(\lambda) = (\phi_w - \phi_{w/o})|_{\lambda}, \qquad (26)$$

where ϕ_w and $\phi_{w/o}$ are the phases in Eq. (24), adjusted with and without including the induced plasmonic field, respectively.

Figures 11(a), 12(a), and 13(a) show the retrieval of the plasmonic field enhancement η defined in Eq. (4) and plotted in Figs. 3(a), 4(a), and 5(a), respectively, as a function of the streaking-pulse wavelength λ for 10-nm diameter Au, Ag, and Cu nanospheres, respectively. The solid red lines show the electric field-strength enhancement $\eta(\mathbf{r}_p)$ obtained using Mie theory at the poles $\mathbf{r}_p$ of the nanospheres. The dashed red lines show the field-strength enhancement $\overline{\eta(\mathbf{r})}$, averaged over the nanosphere surface with the weight factor $|\cos\theta|^2$, approximating the relative contributions of photoelectrons emitted at different angles as dipolar. The blue markers show the streaking-oscillation-amplitude enhancement $\eta_{\rm streak}$ we retrieved from our calculated spectra by using Eqs. (24) and (25). The retrieved streaking-oscillation amplitude enhancement is in good agreement with the averaged plasmonic field-strength

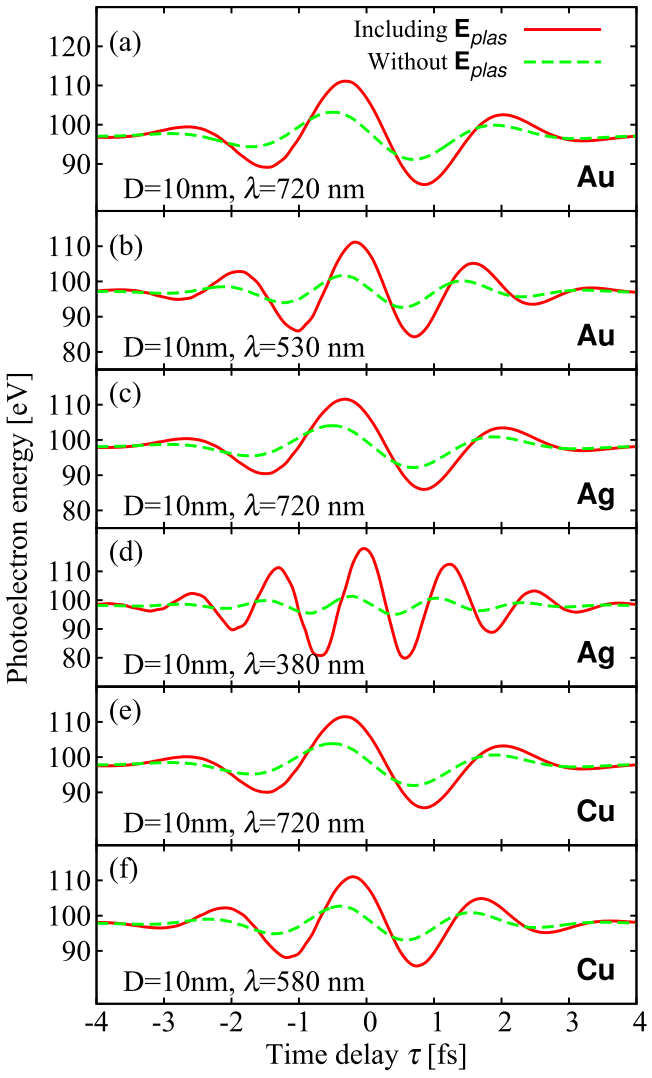

FIG. 10. Centers of energy of streaked photoelectron spectra for 10-nm diameter [(a) and (b)] Au, [(c) and (d)] Ag, and [(e) and (f)] Cu nanospheres, including (red solid line) and excluding (green dashed line) the induced plasmonic field $\mathbf{E}_{\rm plas}$ in Eq. (2).

enhancement $\overline{\eta(\mathbf{r})}$. It not only (i) correctly reproduces the shape of the field-enhancement factor for each element as a function of streaking-pulse wavelength, (ii) matches the enhancement maxima at 530 nm for Au, 360 nm for Ag, and 580 nm for Cu, but also (iii) quantitatively reproduces the numerical value of the averaged enhancement $\overline{\eta(\mathbf{r})}$. Ag nanospheres yield the highest averaged amplitude enhancement $\overline{\eta(\mathbf{r})} \approx 8$, while for Au and Cu nanospheres we find $\overline{\eta(\mathbf{r})} \approx 3$.

Figures 11(b), 12(b), and 13(b) show the retrieval of the plasmonic phase shifts as a function of the streaking-pulse wavelength for 10-nm diameter Au, Ag, and Cu nanospheres, respectively. The red solid lines show the relative plasmonic phase shift,

$$\varphi_{\rm Mie}(\lambda) = \phi_{\rm tot}(\mathbf{r}_p)|_{\lambda} - \phi_{\rm tot}(\mathbf{r}_p)|_{720\,\rm nm}, \qquad (27)$$

obtained using Mie theory at the nanosphere poles $\mathbf{r}_p$ and defined as the phase shift caused by the induced plasmonic field for a central streaking-field wavelength λ, $\phi_{\rm tot}(\mathbf{r}_p)|_{\lambda}$, relative to

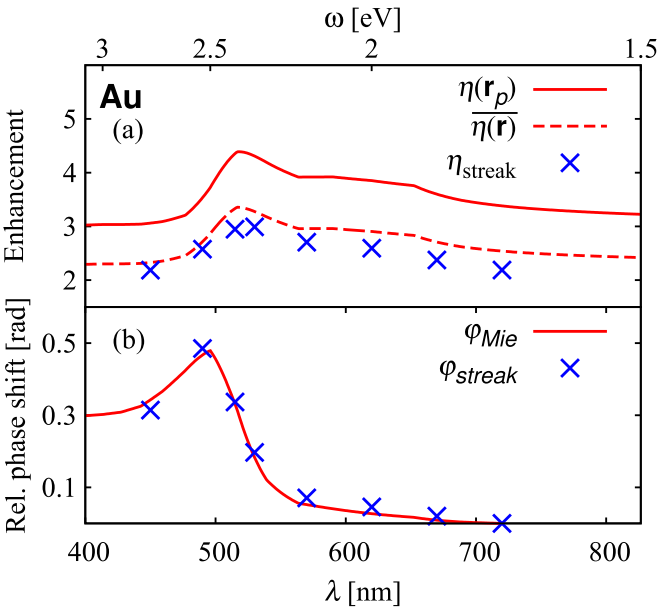

FIG. 11. Plasmonic amplitude-enhancement and phase-shift retrieval for 10-nm diameter Au nanospheres from streaked photoemission spectra. (a) Plasmonic field enhancement η defined in Eq. (4), as predicted by classical electrodynamics: $\eta(\mathbf{r}_p)$ (solid red line) gives values at the nanosphere poles; $\overline{\eta(\mathbf{r})}$ (dashed red line) gives the field-strength enhancement, dipole-averaged over the nanosphere surface. Blue markers indicate the retrieved field-strength enhancement $\eta_{\text{streak}}(\lambda)$ defined in Eq. (25). (b) Plasmonic phase shift $\varphi_{\text{Mie}}(\lambda)$ according to Eq. (27) as predicted by classical electrodynamics at the nanosphere poles (solid red line). Blue markers show the retrieved plasmonic phase-shift difference $\varphi_{\text{streak}}(\lambda)$ defined in Eq. (26) as a function of the streaking-pulse wavelength.

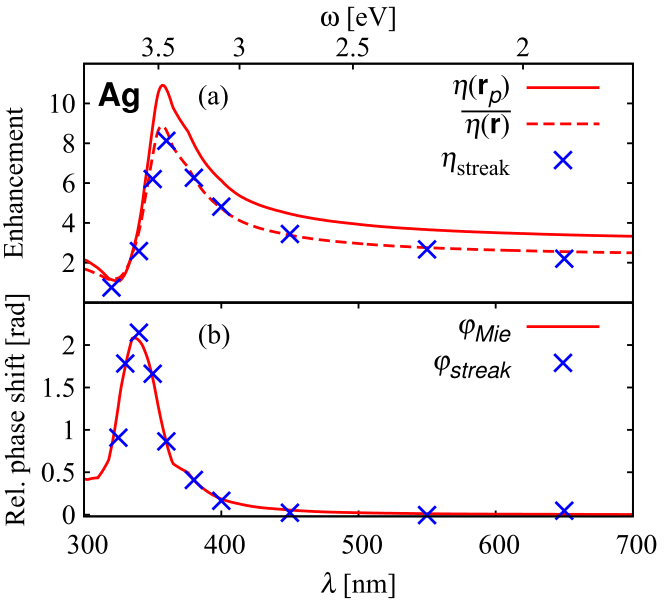

FIG. 12. Same as Fig. 11 for Ag nanospheres.

the induced plasmonic phase shift at $\lambda = 720$ nm [cf. Eq. (2)]. In contrast to the averaged field-strength enhancement, averaging the phase shift over the surface with the same weight factor $|\cos\theta|^2$ does not have a noticeable effect on φ_{Mie}. This is due to the fact that as long as the nanosphere is sufficiently small compared to the streaking-pulse wavelength, the phase shift is approximately homogeneous near the nanosphere surface.

The blue markers in Figs. 11(b), 12(b), and 13(b) show

$$\varphi_{\text{streak}}(\lambda) = \Delta\phi_{\text{streak}}(\lambda) - \Delta\phi_{\text{streak}}(720\text{ nm}), \tag{28}$$

that is, the streaking-phase shifts $\Delta\phi_{\text{streak}}(\lambda)$ defined in Eq. (26) relative to their values at $\lambda = 720$ nm. We retrieved φ_{streak} by fitting Eq. (24) to our calculated streaked spectra. For all three materials, the retrieved relative phase shifts are in excellent agreement with the prediction of classical electrodynamics ("Mie theory"). In particular, the retrieved phase differences accurately reproduce (i) the distinct plasmon resonance peak for Ag [Fig. 12(b)], (ii) the steplike shape of the relative phase shift as a function of streaking-pulse wavelength for Cu [Fig. 13(b)], and (iii) a combination of both step and peak structure for Au [Fig. 11(b)].

The successful retrieval of the plasmonic phase shifts for all three materials provides strong evidence for the accumulation of streaking-wavelength-independent contributions $\Delta\phi_{\text{prop}}$ during the propagation of photoelectrons, leaving the plasmonic phase shift in the electric field, $\phi_{\text{tot}}(\mathbf{r}_p,\omega)$, as the only λ-dependent component. Writing the net accumulated phase difference in streaked photoelectron spectra as

$$\Delta\phi_{\text{streak}}(\lambda) = \phi_{\text{tot}}(\mathbf{r}_p)|_\lambda + \Delta\phi_{\text{prop}}, \tag{29}$$

and taking the difference of Eq. (29) for any given λ and $\lambda = 720$ nm yields

$$\varphi_{\text{streak}}(\lambda) = \varphi_{\text{Mie}}(\lambda). \tag{30}$$

This confirms our numerical evidence presented above that induced plasmonic-field information can be reconstructed from streaked photoelectron spectra.

The plasmonic streaking phase shift $\varphi_{\text{streak}}(\lambda)$ can be assigned to the photoemission time delay $\varphi_{\text{streak}}(\lambda)/\omega$ induced by the collective electronic response of the nanoparticle to the

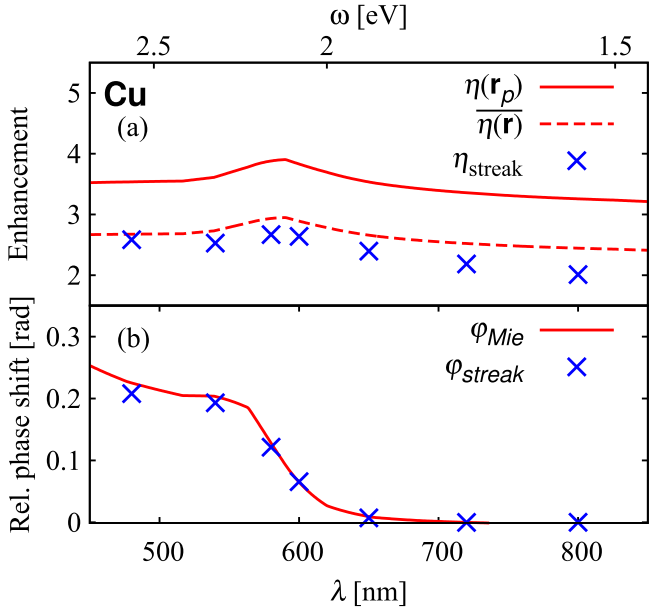

FIG. 13. Same as Fig. 11 for Cu nanospheres.

streaking pulse. Maximal streaking phase shifts of 0.5 rad for Au, 2 rad for Ag, and 0.2 rad for Cu correspond to streaking time delays of 140 as, 380 as, and 60 as, respectively.

In Sec. II A we demonstrated that the magnitude of the plasmonic field enhancement and phase shift are related to the dipole surface plasmon-resonance and interband transitions. The reconstruction of plasmonic field enhancements and phase shifts from attosecond streaked photoelectron spectroscopy may thus provide a not-yet-explored way of studying not only the dielectric response of nanoparticles, but also more intricate properties of their electronic structure, such as interband transitions.

IV. CONCLUSION

We developed a quantum-mechanical model to numerically simulate streaked photoelectron emission from metallic nanospheres and used this method to simulate streaked photoelectron spectra from Au, Ag, and Cu nanospheres. Our study of plasmonic streaking-oscillation-amplitude enhancements and phase shifts revealed in streaked photoemission spectra, relative to simulated spectra that exclude the induced plasmonic field, show how plasmonic near-field information of metallic nanospheres can be retrieved from streaked electron spectra. Our comparative study of element-specific differences in streaking-oscillation-amplitude enhancements and phase shifts reveals the different dielectric properties of the three transition metals. This further substantiates the potential of streaked photoelectron spectroscopy for imaging plasmonic near fields, as well as the dielectric response, surface plasmon resonances, and interband transitions of different materials.

ACKNOWLEDGMENTS

This work was supported in part by the U.S. National Science Foundation (NSF) Experimental Program to Stimulate Competitive Research (EPSCoR) (including funds for investigating laser-induced electric-field enhancement near nanostructures), the NSF under Award No. PHY 1464417 (including theory development for photoemission from surfaces), and the Chemical Sciences, Geosciences, and Biosciences Division, Office of Basic Energy Sciences, Office of Science, U.S. Department of Energy (including attosecond interferometry and photoemission from atoms in spatially varying external fields).

[1] M. I. Stockman, Phys. Today **64**(2), 39 (2011); Opt. Express **19**, 22029 (2011).
[2] S. Law, L. Yu, A. Rosenberg, and D. Wasserman, Nano Lett. **13**, 4569 (2013).
[3] F. Krausz and M. I. Stockman, Nat. Photonics **8**, 205 (2014).
[4] S. Zherebtsov, T. Fennel, J. Plenge, E. Antonsson, I. Znakovskaya, A. Wirth, O. Herrwerth, F. Süßmann, C. Peltz, I. Ahmad, S. A. Trushin, V. Pervak, S. Karsch, M. J. J. Vrakking, B. Langer, C. Graf, M. I. Stockman, F. Krausz, E. Rühl, and M. F. Kling, Nat. Phys. **7**, 656 (2011).
[5] F. Kelkensberg, A. F. Koenderink, and M. J. J. Vrakking, New J. Phys. **14**, 093034 (2012).
[6] J. Li, E. Saydanzad, and U. Thumm, Phys. Rev. A **94**, 051401 (2016).
[7] M. I. Stockman, M. F. Kling, U. Kleineberg, and F. Krausz, Nat. Photonics **1**, 539 (2007).
[8] A. Kinkhabwala, Z. Yu, S. Fan, Y. Avlasevich, K. Müllen, and W. E. Moerner, Nat. Photonics **3**, 654 (2009).
[9] S. L. Stebbings, F. Süßmann, Y. Y. Yang, A. Scrinzi, M. Durach, M. I. Stockman, and M. F. Kling, New J. Phys. **13**, 073010 (2011).
[10] E. Skopalová, D. Y. Lei, T. Witting, C. Arrell, F. Frank, Y. Sonnefraud, S. A. Maier, J. W. G. Tisch, and J. P. Marangos, New. J. Phys. **13**, 083003 (2011).
[11] M. Becker, W. Huang, H. Batelaan, E. J. Smythe, and F. Capasso, Ann. der Phys. (Berlin) **525**, L6 (2013).
[12] S. Kim, J. Jin, Y.-J. Kim, I.-Y. Park, Y. Kim, and S.-W. Kim, Nature (London) **485**, E1 (2012).
[13] P. Dombi, A. Hörl, P. Rácz, I. Márton, A. Trügler, J. R. Krenn, and U. Hohenester, Nano Lett. **13**, 674 (2013).
[14] E. Le Ru and P. Etchegoin, *Principles of Surface-Enhanced Raman Spectroscopy and Related Plasmonic Effects* (Elsevier, Oxford, 2008).
[15] M. T. Sheldon, J. van de Groep, A. M. Brown, A. Polman, and H. A. Atwater, Science **346**, 828 (2014).
[16] X. Zhang, Y. L. Chen, R.-S. Liu, and D. P. Tsai, Rep. Prog. Phys. **76**, 046401 (2013).
[17] W. Chen, C. Ayala-Orozco, N. C. Biswal, C. Perez-Torres, M. Bartels, R. Bardhan, G. Stinnet, X.-D. Liu, B. Ji, A. Deorukhkar, L. V. Brown, S. Guha, R. G. Pautler, S. Krishnan, N. J. Halas, and A. Joshi, Nanomedicine **9**, 1209 (2014).
[18] S. A. Maier and H. A. Atwater, J. Appl. Phys. **98**, 011101 (2005).
[19] F. Süßmann and M. F. Kling, Phys. Rev. B **84**, 121406 (2011).
[20] A. G. Borisov, P. M. Echenique, and A. K. Kazansky, New J. Phys. **14**, 023036 (2012).
[21] J. S. Prell, L. J. Borja, D. M. Neumark, and S. R. Leone, Ann. der Phys. (Berlin) **525**, 151 (2013).
[22] B. Förg, J. Schötz, F. Süßmann, M. Förster, M. Krüger, B. Ahn, W. A. Okell, K. Wintersperger, S. Zherebtsov, A. Guggenmos, V. Pervak, A. Kessel, S. A. Trushin, A. M. Azzeer, M. I. Stockman, D. Kim, F. Krausz, P. Hommelhoff, and M. F. Kling, Nat. Commun. **7**, 11717 (2016).
[23] A. H. Zewail, J. Phys. Chem. A **104**, 5660 (2000).
[24] U. Thumm, T. Niederhausen, and B. Feuerstein, Phys. Rev. A **77**, 063401 (2008), and references therein.
[25] S. De, M. Magrakvelidze, I. A. Bocharova, D. Ray, W. Cao, I. Znakovskaya, H. Li, Z. Wang, G. Laurent, U. Thumm, M. F. Kling, I. V. Litvinyuk, I. Ben-Itzhak, and C. L. Cocke, Phys. Rev. A **84**, 043410 (2011).
[26] R. Kienberger, E. Goulielmakis, M. Uiberacker, A. Baltuska, V. Yakovlev, F. Bammer, A. Scrinzi, Th. Westerwalbesloh, U. Kleineberg, U. Heinzmann, M. Drescher, and F. Krausz, Nature (London) **427**, 817 (2004).
[27] M. Schultze, M. Fieß, N. Karpowicz, J. Gagnon, M. Korbman, M. Hofstetter, S. Neppl, A. L. Cavalieri, Y. Komninos, Th. Mercouris, C. A. Nicolaides, R. Pazourek, S. Nagele, J. Feist, J. Burgdörfer, A. M. Azzeer, R. Ernstorfer, R. Kienberger, U.

Kleineberg, E. Goulielmakis, F. Krausz, and V. S. Yakovlev, Science **328**, 1658 (2010).
[28] K. Klünder, J. M. Dahlström, M. Gisselbrecht, T. Fordell, M. Swoboda, D. Guénot, P. Johnsson, J. Caillat, J. Mauritsson, A. Maquet, R. Taïeb, and A. L'Huillier, Phys. Rev. Lett. **106**, 143002 (2011).
[29] D. Guénot, K. Klünder, C. L. Arnold, D. Kroon, J. M. Dahlström, M. Miranda, T. Fordell, M. Gisselbrecht, P. Johnsson, J. Mauritsson, E. Lindroth, A. Maquet, R. Taïeb, A. L'Huillier, and A. S. Kheifets, Phys. Rev. A **85**, 053424 (2012).
[30] S. R. Leone, C. W. McCurdy, J. BurgdÖrfer, L. S. Cederbaum, Z. Chang, N. Dudovich, J. Feist, C. H. Greene, M. Ivanov, R. Kienberger, U. Keller, M. F. Kling, Z. Loh, T. Pfeifer, A. N. Pfeiffer, R. Santra, K. Schafer, A. Stolow, U. Thumm, and M. J. J. Vrakking, Nat. Photonics **8**, 162 (2014).
[31] U. Thumm, Q. Liao, E. M. Bothschafter, F. Süßmann, M. F. Kling, and R. Kienberger, in *Fundamentals of Photonics and Physics*, edited by D. L. Andrew (Wiley, New York, 2015), Chap. 13.
[32] M. Krüger, M. Schenk, M. Förster, and P. Hommelhoff, J. Phys. B **45**, 074006 (2012).
[33] A. L. Cavalieri, N. Müller, Th. Uphues, V. S. Yakovlev, A. Baltuška, B. Horvath, B. Schmidt, L. Blümel, R. Holzwarth, S. Hendel, M. Drescher, U. Kleineberg, P. M. Echenique, R. Kienberger, F. Krausz, and U. Heinzmann, Nature (London) **449**, 1029 (2007).
[34] C. Lemell, B. Solleder, K. Tőkési, and J. Burgdörfer, Phys. Rev. A **79**, 062901 (2009).
[35] Q. Liao and U. Thumm, Phys. Rev. A **89**, 033849 (2014).
[36] S. Neppl, R. Ernstorfer, A. L. Cavalieri, C. Lemell, G. Wachter, E. Magerl, E. M. Bothschafter, M. Jobst, M. Hofstetter, U. Kleineberg, J. V. Barth, D. Menzel, J. Burgdörfer, P. Feulner, F. Krausz, and R. Kienberger, Nature (London) **517**, 342 (2015).
[37] L. Miaja-Avila, C. Lei, M. Aeschlimann, J. L. Gland, M. M. Murnane, H. C. Kapteyn, and G. Saathoff, Phys. Rev. Lett. **97**, 113604 (2006).
[38] G. Saathoff, L. Miaja-Avila, M. Aeschlimann, M. M. Murnane, and H. C. Kapteyn, Phys. Rev. A **77**, 022903 (2008).
[39] R. Locher, L. Castiglioni, M. Lucchini, M. Greif, L. Gallmann, J. Osterwalder, M. Hengsberger, and U. Keller, Optica **2**, 405 (2015).
[40] Z. Tao, C. Chen, T. Szilvási, M. Keller, M. Mavrikakis, H. Kapteyn, and M. Murnane, Science **353**, 62 (2016).
[41] M. J. Ambrosio and U. Thumm, Phys. Rev. A **94**, 063424 (2016).
[42] Q. Liao and U. Thumm, Phys. Rev. Lett. **112**, 023602 (2014).
[43] A. K. Kazansky and P. M. Echenique, Phys. Rev. B **81**, 193413 (2010).
[44] C.-H. Zhang and U. Thumm, Phys. Rev. A **84**, 065403 (2011).
[45] M. Lupetti, J. Hengster, T. Uphues, and A. Scrinzi, Phys. Rev. Lett. **113**, 113903 (2014).
[46] M. Lucchini, A. Ludwig, L. Kasmi, L. Gallmann, and U. Keller, Opt. Express **23**, 8867 (2015).
[47] K. T. Kim, D. M. Villeneuve, and P. B. Corkum, Nat. Photonics **8**, 187 (2014).
[48] E. Saydanzad, J. Li, and U. Thumm (unpublished).
[49] G. Mie, Ann. Phys. **330**, 377 (1908).
[50] J. A. Stratton, *Electromagnetic Theory* (Wiley, Hoboken, 2007).
[51] D. W. Lynch and D. R. Hunter, in *Handbook of Optical Constants of Solids*, edited by E. D. Palik (Academic Press, Orlando, 1985), p. 275.
[52] H. Ehrenreich and H. R. Philipp, Phys. Rev. **128**, 1622 (1962).
[53] H. Wang, F. Tam, N. K. Grady, and N. J. Halas, J. Phys. Chem. B **109**, 18218 (2005).
[54] S. A. Maier, *Plasmonics: Fundamentals and Applications* (Springer, New York, 2007).
[55] S. Link and M. A. El-Sayed, J. Phys. Chem. B **103**, 4212 (1999).
[56] U. Thumm, P. Kürpick, and U. Wille, Phys. Rev. B **61**, 3067 (2000).
[57] E. Merzbacher, *Quantum Mechanics* (Wiley, New York, 1998).
[58] W. M. Haynes, *CRC Handbook of Chemistry and Physics*, 96th ed. (CRC Press, Boca Raton, 2015).
[59] A. Sekiyama, J. Yamaguchi, A. Higashiya, M. Obara, H. Sugiyama, M. Y. Kimura, S. Suga, S. Imada, I. A. Nekrasov, M. Yabashi, K. Tamasaku, and T. Ishikawa, New J. Phys. **12**, 043045 (2010).
[60] S. Tanuma, C. J. Powell, and D. R. Penn, Surf. Interface Anal. **43**, 689 (2011).
[61] J. Stöhr, F. R. McFeely, G. Apai, P. S. Wehner, and D. A. Shirley, Phys. Rev. B **14**, 4431 (1976).